Journal of Computational Physics **174,** 438–459 (2001)
doi:10.1006/jcph.2001.6926, available online at http://www.idealibrary.com on IDEAL®

The Nonlinear Evolution of Vortex Sheets with Surface Tension in Axisymmetric Flows

Qing Nie

Department of Mathematics, University of California at Irvine, Irvine, California 92697-3875
E-mail: qnie@math.uci.edu

Received March 27, 2000; revised August 3, 2001

The presence of surface tension for interfacial flows usually leads to severe stability constraints for explicit time integration methods. Moreover, the nonlocality and nonlinearity of the high-order terms make the application of implicit methods difficult. In this paper, a computational strategy is presented for computing the motion of fluid interfaces with surface tension in axisymmetric flows using boundary integral techniques. This method is based on adaptive quadratures for the principal-value integrals and a small-scale decomposition for the treatment of surface tension through a vector-potential formulation. A study of the method is conducted in the context of vortex sheet evolution with surface tension in axisymmetric flows. The method is found to be accurate, efficient, and robust. Numerical simulations indicate that the dynamics of vortex sheets with surface tension frequently result in topological singularities (i.e., self-intersection). Away from the axis of symmetry, these singularities are similar to those found in the two-dimensional flows. Singularities occurring near the axis of symmetry take a different form.

Key Words: free surfaces in axisymmetric flows; surface tension; vortex sheet.

1. INTRODUCTION

Interfaces between inviscid, immiscible liquids are typically unstable. In the absence of stabilizing effects such as surface tension or viscosity, interfaces rapidly form curvature singularities in finite time due to the Kelvin–Helmholtz (shear) instability [1]. Surface tension in principle acts as a regularization of this instability. This can be seen through a linear analysis: the surface tension prevents the growth of small perturbations above a critical wavenumber. However, in axisymmetric and three-dimensional geometries, the inclusion of surface tension introduces another source of instability: the Rayleigh instability. The case of a vortex sheet stands as an important fundamental example of fluid motion involving interfaces. In the case that we focus on in this paper, the vortex sheet separates

0021-9991/01 $35.00

two immiscible and density-matched fluids, and there is competition only between the shear instability and the surface tension.

Boundary integral techniques provide a popular approach to computing the evolution of interfaces with surface tension. One of the major features of boundary integral techniques is that the equations of motion may be reposed entirely along the interface, thus reducing the complexity of the problem by one dimension. In addition, boundary integral techniques are particularly convenient for the treatment of surface tension that requires the calculation of curvature [2–4].

For two-dimensional flows, surface tension has now been included in numerical studies of many free-surface problems. These include the study of the rising gas bubble [5], vortex sheets with surface tension [6–11], the Rayleigh–Taylor instability [7, 8, 12, 13], and the generation of capillary waves [14]. See the recent review article by Hou *et al.* [4].

Until recently, it has been problematic to obtain stable numerical methods, even in two dimensions. In the context of the motion of vortex sheets with surface tension, Baker and Nachbin [9] have demonstrated through linear analysis and nonlinear computations that the main cause of instability (the growth of the sawtooth mode) is the failure of the mesh to represent vorticity created by the surface tension. They then developed a stable numerical method in which this instability is removed by using a midpoint rule to approximate the boundary integrals. Independently, Beale *et al.* [15, 16], and subsequently Ceniceros and Hou [13] analyzed this numerical instability using a slightly different formulation and proposed alternative stable methods.

In addition, the presence of surface tension requires small time steps when an explicit method is used, and results in a strong stability constraint, $\Delta t \leq C(\Delta s)^{3/2}$, where Δs is the smallest arclength between two computational mesh points on the sheet. This is due to the interface curvature that appears in the boundary condition for the vortex sheet strength. As an example, an explicit method based on Lagrangian motion accumulates the markers near a stagnation point on the interface (reducing Δs as a result) and forces the use of an ever-decreasing time step [7–9, 16].

In 1994, Hou *et al.* (HLS94) [10] introduced a new formulation and methods based on a *small-scale decomposition* of nonlinear equations. The main idea in this approach is to separate the most singular part (e.g., the part with the highest derivative) of the equation from the rest and treat the singular part implicitly through a change of variable. In particular, the interface location is represented in terms of its local arclength s and its tangent angle θ. The most singular part of the normal velocity of the interface is found to be a Hilbert transformation of the vortex sheet strength, which can be diagonalized in Fourier space. As a result, it can be treated implicitly and efficiently along with the curvature θ_s. The new formulation has all the nice properties of time integration methods that are associated with having a linear highest-order term. The resulting methods do not have the severe stability constraints usually associated with surface tension. This method has been successfully used to study the long-time evolution of vortex sheets with surface tension [11].

In three dimensions, the study of vortex sheet motion has been restricted to the cases without surface tension. There is evidence for the formation of singularities in the axisymmetric geometry [17–19] and for certain three-dimensional perturbations of a plane vortex sheet [20, 21]. In addition, by form-fitting the Fourier coefficients of the numerical solutions, it is found that there exists curvature singularity and that singularity formations in axisymmetric and two-dimensional vortex sheets are very similar [18, 22, 23]. In this paper, we are interested in simulations of vortex sheet motion with *surface tension* in axisymmetric flows.

Computing the motion of vortex sheets in axisymmetric flows using boundary integral methods is more difficult than it is in two dimensions for several reasons. First, the principal-value integrals involve complete elliptic integrals and contain logarithmic singularities. Further, the integrand has large variation near the axis of symmetry [19, 24, 25] when the vortex sheets cross or approach the axis of symmetry. Consequently the design of an accurate quadrature is difficult for axisymmetric flows. For example, the high-order method [26] designed for treating the logarithmic singularities in the integrand in 2-D loses its accuracy near the axis of symmetry and becomes a first-order method [19]. In 1998, Nie and Baker (NB98) [18] introduced a new quadrature technique for axisymmetric flows based on a dipole representation of the vortex sheet through the vector-potential formulation. In this approach, high-order adaptive numerical quadratures are incorporated to ensure the accurate calculation of the principal-value integrals by inserting more quadrature points where the integrand has large variation.

The second major numerical difficulty is the strong time-step stability constraint that arises due to the presence of surface tension. This is similar to the two-dimensional case. Until very recently, this stability constraint has been somewhat modified by regridding the interface markers at every time step or after several time steps and imposing surface smoothing in ad-hoc ways [27–29]. Experience shows that this does not entirely eliminate the stability constraints and it only partially improves the computations.

In this study, we combine the small-scale decomposition technique presented for two-dimensional flows in HLS94 and the strategy using adaptive quadratures for axisymmetric flows in NB98 to develop accurate and efficient methods that can be used to study vortex sheets with surface tension in axisymmetric flows. We note that very recently Ceniceros and Si [30] developed a related algorithm that uses quadratures presented in [19] and the small-scale decomposition technique to study axisymmetric porous media flows. In [30] the effect of small surface tension on the dynamics of an axisymmetric flow is studied.

As shown in HLS94 the central reasons for using the small-scale decomposition technique are that the most singular terms in the equations can be identified, treated implicitly in temporal integration, and computed efficiently. Fortunately, we find this is achievable in the axisymmetric case. In particular, the Lagrangian velocity of the vortex sheet is found to be dominated by a Hilbert transform of vortex sheet strength at small scales, similar to the two-dimensional case. For the surface tension term, the curvature in the axisymmetric geometry is a sum of curvatures in the meridian direction and in the azimuthal direction. At small scales, this sum is dominated by its two-dimensional counterpart, the one from meridian direction, because it contains the highest number of derivatives. In order to treat the terms implicitly in the temporal scheme, we represent the vortex sheet in the meridian plane using the tangent angle θ and equal arclength L similar to the two-dimensional case (HLS94). The velocity for the vortex sheet is computed using a dipole representation through the vector-potential formulation (NB98). Adaptive quadratures are implemented for the sake of efficiency and of accuracy for the calculations of principal-value integrals.

We use this method to calculate the evolution of an initially spherical vortex sheet and study the evolution of the vortex sheet for different values of surface tension and for different choices of the initial vortex sheet strength. The method is found to be robust and accurate. The computations show that the evolution of the vortex sheet sensitively depends on the surface tension. In particular, for small surface tensions, the sheet develops a rolled-up structure and the interface self-intersects (pinches off) away from the axis of symmetry. This type of pinch-off is found to be similar to the analogous pinch-off that occurs in

two-dimensional flows. For large surface tensions, the sheet necks down and the pinch-off occurs at the axis of symmetry ($r = 0$). For this case we notice an overturning of the interface, which is not observed for the two-dimensional flows. For moderately sized surface tensions, the sheet evolves via a combination of spirals, necks, and pinch-offs.

The organization of the paper is as follows. In Section 2, we derive a formulation based on the small-scale decomposition for axisymmetric flows. In Section 3, we describe the numerical techniques and discuss the details of the implementation. In Section 4, we study the accuracy of the numerical method and present the results. In Section 5, we present the conclusions and discussions.

2. FORMULATIONS

For an axisymmetric vortex sheet, we may represent the sheet position, denoted by Γ, as

$$\mathbf{X} = r(\alpha, t)\mathbf{e}_r + z(\alpha, t)\mathbf{e}_z, \tag{1}$$

using the cylindrical coordinates (r, z). The motion of Γ is given by

$$(r_t, z_t) = V_n\mathbf{n} + T\mathbf{s}, \tag{2}$$

where $\mathbf{n}$ is the inward normal of the sheet with V_n as the inward normal velocity and $\mathbf{s}$ is the tangential direction of the sheet with T as a specified tangential velocity. We remark that the choice of T does not affect the motion of the sheet Γ, and it only affects the definition of α.

In the Lagrangian frame, the velocity of the sheet is given by the Biot–Savart integral [31]

$$\bar{u}_r = \frac{1}{4\pi r} \mathbb{P} \int \gamma'(z' - z) B_0(\alpha, \alpha')(F(k) + B_1(\alpha, \alpha')E(k))\, d\alpha', \tag{3}$$

$$\bar{u}_z = \frac{1}{4\pi} \mathbb{P} \int \gamma' B_0(\alpha, \alpha')(F(k) + B_2(\alpha, \alpha')E(k))\, d\alpha', \tag{4}$$

where $F(k)$ and $E(k)$ are the complete elliptic integrals of the first and second kind, respectively, with

$$k^2 = \frac{4rr'}{(z - z')^2 + (r + r')^2}, \quad B_0(\alpha, \alpha') = \frac{2}{((z - z')^2 + (r + r')^2)^{1/2}}, \tag{5}$$

$$B_1(\alpha, \alpha') = -\frac{(z' - z)^2 + r'^2 + r^2}{(z - z')^2 + (r - r')^2}, \quad B_2(\alpha, \alpha') = \frac{r'^2 - r^2 - (z' - z)^2}{(z - z')^2 + (r - r')^2}, \tag{6}$$

where $r' = r(\alpha', t)$, etc. The vortex sheet strength $\gamma(\alpha, t) \equiv \mu_\alpha(\alpha, t)$ can be determined through the dipole sheet strength μ (NB98), which evolves via

$$\frac{\partial \mu}{\partial t} = (T - \mathbf{s} \cdot \bar{\mathbf{u}})\mu_s - \sigma\kappa_{mean}, \tag{7}$$

where $s_\alpha \equiv \sqrt{r_\alpha^2 + z_\alpha^2}$ and $\kappa_{mean} \equiv \kappa + \kappa_\infty$ is twice the mean curvature. Here κ and κ_∞ are the curvatures in the meridian and azimuthal directions, respectively:

$$\kappa = \frac{r_\alpha z_{\alpha\alpha} - r_{\alpha\alpha} z_\alpha}{s_\alpha^3} \quad \kappa_\infty = \frac{z_\alpha}{r s_\alpha}. \tag{8}$$

The normal velocity then is obtained from

$$V_n = \bar{\mathbf{u}} \cdot \mathbf{n}. \tag{9}$$

The choice $T = \mathbf{s} \cdot \bar{\mathbf{u}}$ corresponds to the Lagrangian frame.

The motion of Γ can be reposed in terms of its local arclength derivatives s_α and its tangent angle θ defined implicitly from the definition of the tangent vector,

$$\mathbf{s}(\alpha, t) = (r_\alpha, z_\alpha)/s_\alpha = (\cos\theta(\alpha, t), \sin\theta(\alpha, t)). \tag{10}$$

Then θ and s_α satisfy

$$s_{\alpha t} = T_\alpha - \theta_\alpha V_n \tag{11}$$

$$\theta_t = \frac{V_{n\alpha} + T\theta_\alpha}{s_\alpha} \tag{12}$$

with T as yet unspecified.

Because κ contains higher derivative of r and z than κ_∞ in κ_{mean}, we obtain, after taking a derivative of Eq. (7) with respect to α,

$$\gamma_t \sim -\sigma\kappa_\alpha, \tag{13}$$

where $f \sim g$ means that the difference between f and g is smoother than f and g. This can be seen by an argument similar to that used for the small-scale decomposition in the two-dimensional case (HLS94).

Next we examine the leading-order behavior for V_n. From the Biot–Savart integrals for $(\bar{u}_r, \bar{u}_z)$, with $\mathbf{n} = (-z_s, r_s)$, we obtain

$$V_n = (\bar{u}_r, \bar{u}_z) \cdot (-z_s, r_s) \sim -\frac{1}{2\pi s_\alpha} \int \frac{\gamma'}{\alpha - \alpha'} \, d\alpha' \quad \text{as } \alpha \to \alpha'. \tag{14}$$

Here, we have used the fact that for $r \equiv r(\alpha) \neq 0$ the leading order terms of the integrands in (3) and (4) are

$$-\frac{2r\gamma' z_\alpha}{s_\alpha^2(\alpha' - \alpha)} \quad \text{and} \quad \frac{2\gamma' r_\alpha}{s_\alpha^2(\alpha' - \alpha)}, \tag{15}$$

respectively.

Consequently, we regroup V_n as

$$V_n = -\frac{1}{2s_\alpha}\mathcal{H}(\gamma) + \text{remainder}, \tag{16}$$

where $\mathcal{H}$ is the Hilbert transform and the remaining term is smoother than the Hilbert transform.

Using the fact that $\theta_s = \kappa$, we obtain the small-scale decomposition equation for the axisymmetric vortex sheet,

$$\theta_t = -\frac{1}{2}\frac{1}{s_\alpha}\left(\frac{1}{s_\alpha}\mathcal{H}(\gamma)\right)_\alpha + P \tag{17}$$

$$\gamma_t = -\sigma\left(\frac{\theta_\alpha}{s_\alpha}\right)_\alpha + Q, \tag{18}$$

where

$$P \equiv \frac{1}{2}\frac{1}{s_\alpha}\left(\frac{1}{s_\alpha}\mathcal{H}(\gamma)\right)_\alpha + \frac{V_{n\alpha} + T\theta_\alpha}{s_\alpha} \tag{19}$$

$$Q \equiv ((T - s\cdot\bar{\mathbf{u}})\mu_s - \sigma\kappa_\infty)_\alpha. \tag{20}$$

The form of the equations is exactly the same as in the two-dimensional case except that P and Q are different. In the two-dimensional case, P and Q involve only Birkhoff–Rott integrals while for the axisymmetric case κ_∞ is present in Q. Moreover, V_n and $\bar{\mathbf{u}}$ are more difficult to compute.

3. NUMERICAL METHODS

Following HLS94, we use a semiimplicit temporal scheme for Eq. (17) and (18). To avoid solving a linear system during the time integration, we require s_α to be a function of time only,

$$s_\alpha(\alpha, t) = \frac{L(t)}{2\pi} \equiv 1/M(t). \tag{21}$$

This can be achieved by choosing the special tangential velocity

$$T(\alpha, t) = \frac{\alpha}{2\pi}\int_0^{2\pi} \theta_{\alpha'} V_n \, d\alpha' - \int_0^{\alpha} \theta_{\alpha'} V_n \, d\alpha'. \tag{22}$$

Consequently, Eq. (11) for s_α becomes

$$L_t = \int_0^{2\pi} \theta_{\alpha'} V_n \, d\alpha'. \tag{23}$$

Denote $\hat{f}(k)$ to be the Fourier coefficient of f. By applying the Crank–Nicholson discretization to the leading-order term in the Fourier space in Eq. (17) and (18), we obtain the following diagonalized system in Fourier space:

$$\frac{\hat{\theta}(k)^{n+1} - \hat{\theta}(k)^{n-1}}{2\Delta t} = -\frac{|k|}{4}((M^{n+1})^2\hat{\gamma}(k)^{n+1} + (M^{n-1})^2\hat{\gamma}(k)^{n-1}) + \hat{P}^n(k) \tag{24}$$

$$\frac{\hat{\gamma}(k)^{n+1} - \hat{\gamma}(k)^{n-1}}{2\Delta t} = \sigma\frac{k^2}{2}(M^{n+1}\hat{\theta}(k)^{n+1} + M^{n-1}\hat{\theta}(k)^{n-1}) + \hat{Q}^n(k). \tag{25}$$

The quantities $\hat{\theta}^{n+1}(k)$ and $\hat{\gamma}^{n+1}(k)$ can be calculated explicitly by inverting a 2×2 matrix.

L should be updated by an explicit method such as the second-order Adams–Bashforth discretization of Eq. (23). The computations of θ and γ will require this updated L. Once L and θ are known, we can numerically integrate Eq. (10) to obtain (r, z). Similarly, we can calculate μ through the numerical integration of γ.

The above formulation is the same as in HLS94 except that V_n, P, and Q are different. For P and Q, the essential parts involve V_n and $\bar{\mathbf{u}}$. As studied in NB98, one of the major challenges of using the boundary integral technique to compute free surfaces in an axisymmetric flow is the accurate evaluations of the velocity integrals. This is particularly true for the motion of vortex sheets with small surface tensions σ because for $\sigma = 0$ the governing equation is ill-posed. In NB98, we developed a very efficient and accurate strategy to compute V_n and $\bar{\mathbf{u}}$ based on a vector-potential formulation with an adaptive quadrature. We implement the same method for $\sigma \neq 0$ in this paper. Below, we present a brief sketch of this technique.

The normal velocity is computed through a vector potential by

$$V_n = \frac{\psi_\alpha}{r} \tag{26}$$

and (3) and (4) can be rewritten as

$$\bar{u}_r = \left(\phi_\alpha r_\alpha - \frac{\psi_\alpha}{r} z_\alpha\right)\frac{1}{s_\alpha^2}, \tag{27}$$

$$\bar{u}_z = \left(\phi_\alpha z_\alpha + \frac{\psi_\alpha}{r} r_\alpha\right)\frac{1}{s_\alpha^2}, \tag{28}$$

where the potential function ϕ and the vector potential function ψ have the following integral representations,

$$\phi(\alpha) = \frac{1}{4\pi} \mathop{\mathrm{P}\!\!\!\!\!\!\int} (\mu' - \mu) B_0(\alpha, \alpha')(z'_\alpha F(k) + C_1(\alpha, \alpha') E(k))\, d\alpha' + \frac{1}{2}\mu, \tag{29}$$

$$\psi(\alpha) = \frac{1}{4\pi} \mathop{\mathrm{P}\!\!\!\!\!\!\int} (\mu' - \mu) B_0(\alpha, \alpha')([r'_\alpha r' - z'_\alpha (z - z')]F(k) + C_2(\alpha, \alpha') E(k))\, d\alpha', \tag{30}$$

with

$$C_1(\alpha, \alpha') = -\frac{(z - z')[z'_\alpha (z - z') - 2r' r'_\alpha] + (r^2 - r'^2) z'_\alpha}{(z - z')^2 + (r - r')^2} \tag{31}$$

and

$$C_2(\alpha, \alpha') = \frac{(z - z')([z'_\alpha (z - z') - r'_\alpha r'](z - z') + z'_\alpha (r^2 + r'^2)) + (r^2 - r'^2) r'_\alpha r'}{(z - z')^2 + (r - r')^2}. \tag{32}$$

The integrands in (29) and (30) exhibit the following asymptotic behavior,

$$-\frac{z_\alpha \mu_\alpha}{r}(\alpha' - \alpha) \ln|\alpha - \alpha'| \quad \text{and} \quad -2\mu_\alpha r, \tag{33}$$

respectively, compared with the pole singularities $1/(\alpha' - \alpha)$ for the integrands in (3) and (4). This property of the integrands allows one to use more sophisticated quadratures to

compute the integrals and improve the accuracy. In particular, the difficulty arising from large variations of the integrand near the axis, $r = 0$, which in turn causes large loss of resolution, can be overcome by inserting more quadrature points around $r = 0$.

One special class of quadratures we employed in NB98 was the Gauss–Kronrod quadrature [32, 33]. The major difference between this quadrature and standard ones is its progressive nature for the construction of the quadrature; i.e., one rule can be generated by adding new points to another Gaussian rule. This progressive property is crucial for any adaptive strategies. In this study, we use a 7- to 15-point, Gauss–Kronrod quadrature. We bisect the integration intervals and estimate the error of the numerical integration over each interval by measuring the difference between the 7-point Gauss quadrature and 15-point Kronrod rule. A globally adaptive strategy is to bisect the interval with the largest error estimate until the error is less than a prescribed tolerance. We used the freely available software package Quadpack [34] to implement this strategy. The recursive formulae [35, p. 297] are used for the evaluation of both $F(k)$ and $E(k)$.

Another strategy, which exploits the logarithmic behavior of the integrands in (29) and (30), is also implemented using Clenshaw–Curtis quadrature [36, 37]. This method is based on an expansion of the integrand in a series of Chebyshev polynomials. The method varies the number of terms in the series to reach a specified level of accuracy, and thus is naturally adaptive.

We approximate the closed surface by a set of boundary nodes along the contour in the (r, z) meridional plane, $(r_i, z_i) \equiv (r(\alpha_i), z(\alpha_i))$ for $i = 1, \ldots, \bar{N}$, where $\alpha_i = i\pi/(\bar{N} - 1)$. We calculate ϕ and ψ at those points, denoted by ϕ_i and ψ_i. Although the integrands in (29) and (30) are continuous when $\alpha = \alpha'$, their derivatives are not. So we split the integrals (29) and (30) into two parts: one integrated from 0 to α_i, another one from α_i to π, with the following form:

$$\int_0^{\pi} f(\alpha, \alpha')\, d\alpha' + \int_0^{\alpha} g_1(\alpha, \alpha') \ln(\alpha - \alpha')\, d\alpha' + \int_{\alpha}^{\pi} g_2(\alpha, \alpha') \ln(\alpha' - \alpha)\, d\alpha'. \quad (34)$$

Next, we employ the Gauss–Kronrod rule on the first integral in (34), and modified Clenshaw–Curtis rule on the second and third integrals in (34). For (r, z) that are not at the collocation point α_i during the integral evaluations, we approximate them through interpolation using a quintic spline [38]. Consequently, the order of the accuracy for this method is $O(\bar{N}^{-6})$.

Once ϕ_i and ψ_i are evaluated, their derivatives are obtained using fast Fourier transformation (FFT). Derivatives such as z_α, r_α are also calculated using FFT. The evaluation of ψ_α / r at $r = 0$ is treated separately by computing $\psi_{\alpha\alpha}/r_\alpha$.

It has been found that for two-dimensional free-surface flows with surface tension [9, 16], using splines for numerical derivatives introduces numerical instability. However, this numerical instability can be suppressed by filtering [16]. In all computations presented, we employ a similar spectral Fourier filter,

$$e^{-c_0(|k|/N)^p} \hat{f}(k), \quad (35)$$

with a cutoff filter [39] which sets all Fourier coefficients below a filter level ϵ_f to zero. We typically chose $c_0 = 10$, $p = 15$, and $\epsilon_f = 10^{-12}$ unless otherwise specified. This filter is implemented at every time step for z, r, and γ; i.e., each Fourier coefficient of z, r, and γ is replaced by Eq. (35) and furthermore, all coefficients below ϵ_f are set to zero.

4. NUMERICAL RESULTS

We follow previous work [17, 40] using a sphere as the initial shape of vortex sheet throughout this paper. The parameterization of the sphere surface is

$$r(\alpha, 0) = \sin(\alpha) \quad z(\alpha, 0) = -\cos(\alpha) \quad \alpha \in [0, \pi]. \tag{36}$$

We first consider

$$\mu(\alpha, 0) = -\cos(\alpha) \quad \alpha \in [0, \pi] \tag{37}$$

as the initial condition for the dipole strength, whose derivative is the vortex sheet strength and $\gamma > 0$ for $r > 0$. This initial condition corresponds to a uniform potential flow past a solid sphere that is instantaneously dissolved at $t = 0$. The vortex sheet at the boundary of the sphere is then allowed to evolve freely. For $\sigma = 0$ this initial condition was studied in NB98, where it was shown that the vortex sheet develops curvature singularities around time $t = 1.09$.

In Fig. 1, the profiles of the axisymmetric vortex sheet are shown at four different times for $\sigma = 0.04$. The results are obtained using $\epsilon_I = 10^{-12}$, $N = 513$, and the time step $\Delta t = 10^{-3}$. ϵ_I denotes the tolerance requirement for the evaluation of various integrals, and N is the total number of points representing the whole surface including the image for $r < 0$.

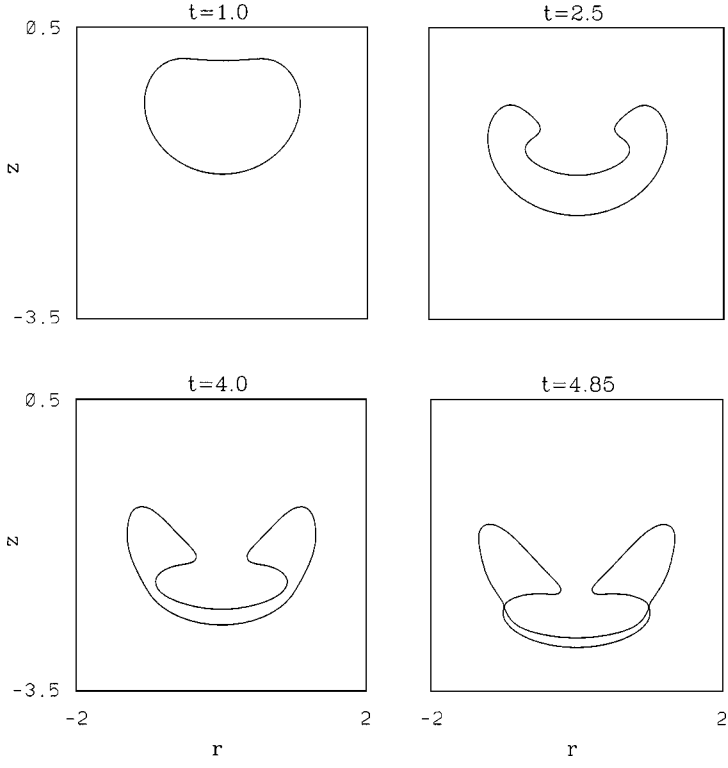

FIG. 1. Evolution of an axisymmetric sheet for $\sigma = 0.04$.

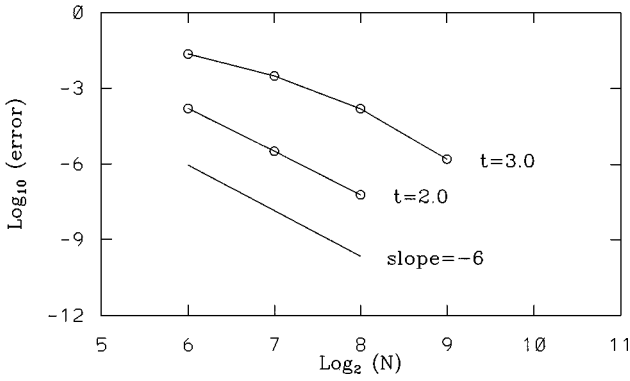

FIG. 2. Log–log plot of the maximum errors as functions of N for the spatial resolution study.

In the presence of surface tension, the evolution of the vortex sheet passes $t = 1.09$ (the singularity time for $\sigma = 0$) and the top part of the sheet moves toward the lower part of the sheet (see Fig. 1). Meanwhile the sheet develops two fingers (only those for $r > 0$) with one moving toward $r = 0$ and the other toward the outer part of the sheet. The code stops when two parts of the sheet collide around $t = 4.85$, and a singularity forms. In a subsequent work [41], we will analyze the singularity behavior in detail.

We establish the accuracy in our computations through a resolution study. First, we consider the influence of the number of collocation points N that represent the interface. We use the maximal difference between the solution calculated using $N = 1025$ and the solution calculated using smaller N as an estimate for the error. We plot the error for $N = 65, 129, 257, 513$ in Fig. 2. Here, the time step is $\Delta t = 10^{-3}$. Since quintic interpolation is used for the adaptive quadratures, the dominant error should be $O(N^{-6})$ if the errors in evaluating the integrals are small compared with all other errors (associated with approximations of the interfaces, interpolations, and derivatives). In Fig. 2, we see almost a straight line for the logarithm of the error at $t = 2$ as a function of N, which is consistent with $O(N^{-6})$ behavior. At the later time $t = 3$, the log of the errors is no longer a straight line. However, the error for larger N still shows $O(N^{-6})$ accuracy.

Next we consider the errors caused by the temporal discretization. Similar to the spatial resolution study, we calculate the maximal difference between the solution computed using $\Delta t = 0.001$ and those using larger Δt. Here, we pick $N = 513$. Since our time integrator has an error of $O(\Delta t^2)$, we should obtain an improvement of accuracy of a factor of 4 whenever Δt is halved. In Fig. 3, the errors are plotted as functions of time for $\Delta t = 0.01, 0.005, 0.0025$. Except at very early times, the errors uniformly decrease with a factor of about 4 as Δt decreases to 0.0025. We note that the errors increase only slowly as the shape of the sheet evolves significantly, which is in contrast to the behavior of the spatial resolution. This indicates that at later times when the sheet deforms the overall resolution of the method is dominated by the spatial resolution.

In Figs. 4 and 5, the mean curvature and vortex sheet strength γ are plotted against α at different times. The physical and computational parameters in these two figures are the same as those in Fig. 1. In both figures, $\alpha = 0$ corresponds to the bottom of the interface at $r = 0$. In Fig. 4, at earlier times there are two positive peaks of the curvature, which correspond to the tips of the two fingers moving toward $r = 0$. The two negative peaks correspond to the fingers moving outward. At $t = 4.85$, another two negative peaks in the curvature develop

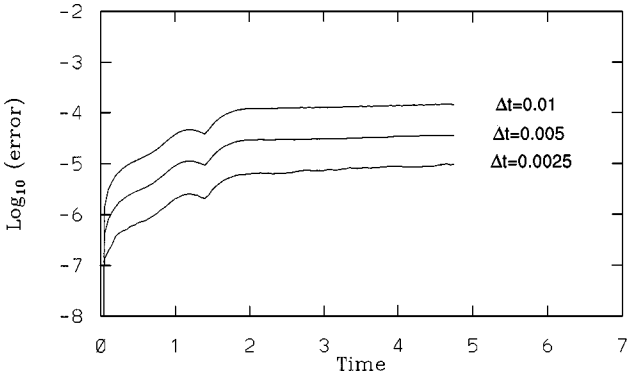

FIG. 3. The maximum errors as functions of time for the temporal resolution study.

near the locations of the pinching on the outer sheet. For the vortex sheet strength at $t = 4.85$ (Fig. 5), the first negative peak starting from $\alpha = 0$ corresponds to the pinching point on the outer sheet, and the positive peak close to π corresponds to the pinching point on the inside interface. This indicates an outward flux of fluid from the bottom of the sheet into the bigger blobs on the top. As a result, the sheet forms a thin and long thread on the bottom with two big blobs on the top.

We now reduce the surface tension to $\sigma = 0.01$ and plot the corresponding evolution of the sheet in Fig. 6. The calculation starts with $N = 513$ and $\Delta t = 10^{-4}$, which are successively refined up to $N = 2049$ and $\Delta t = 10^{-5}$ as time advances. As in the previous case, once

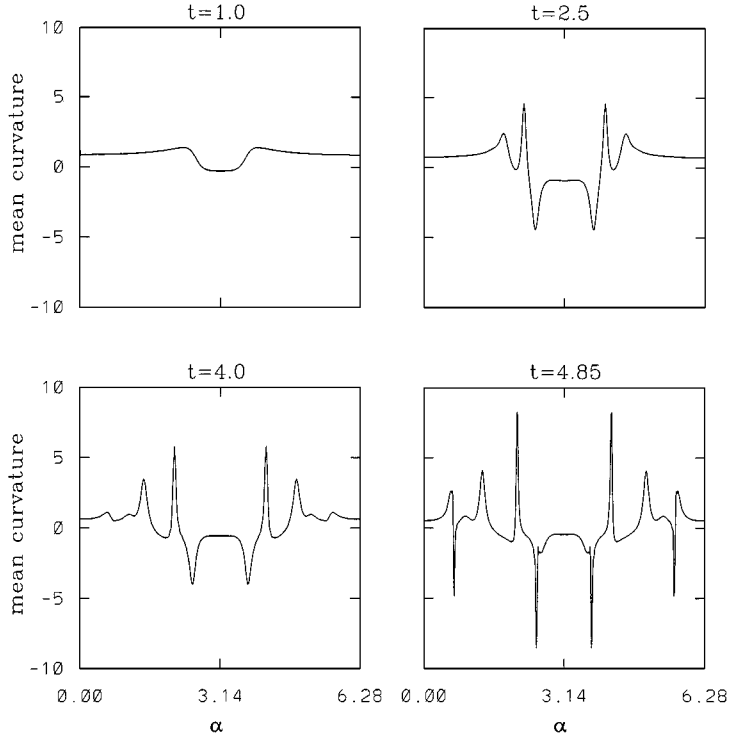

FIG. 4. Mean curvatures vs α at different times for $\sigma = 0.04$.

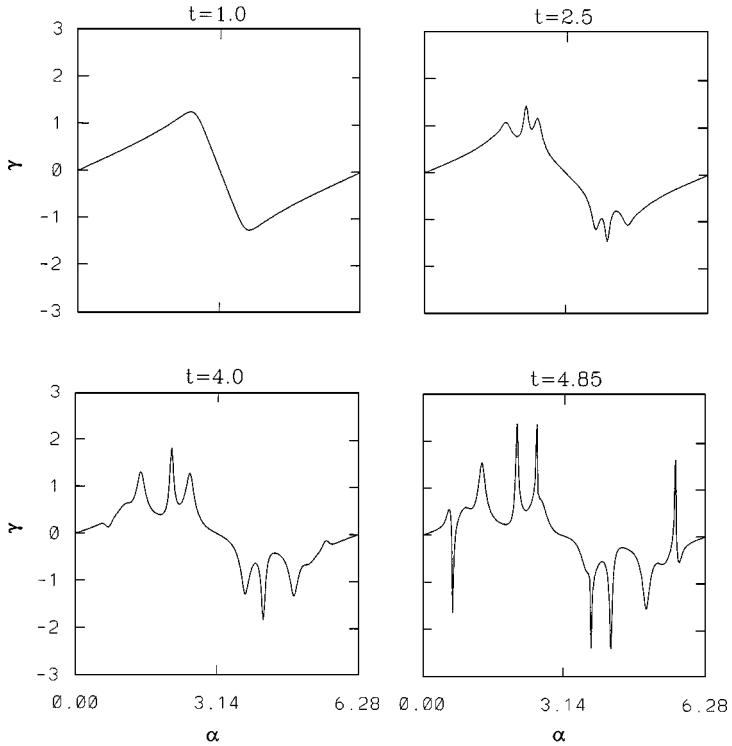

FIG. 5. Vortex sheet strength γ vs α at different times for $\sigma = 0.04$.

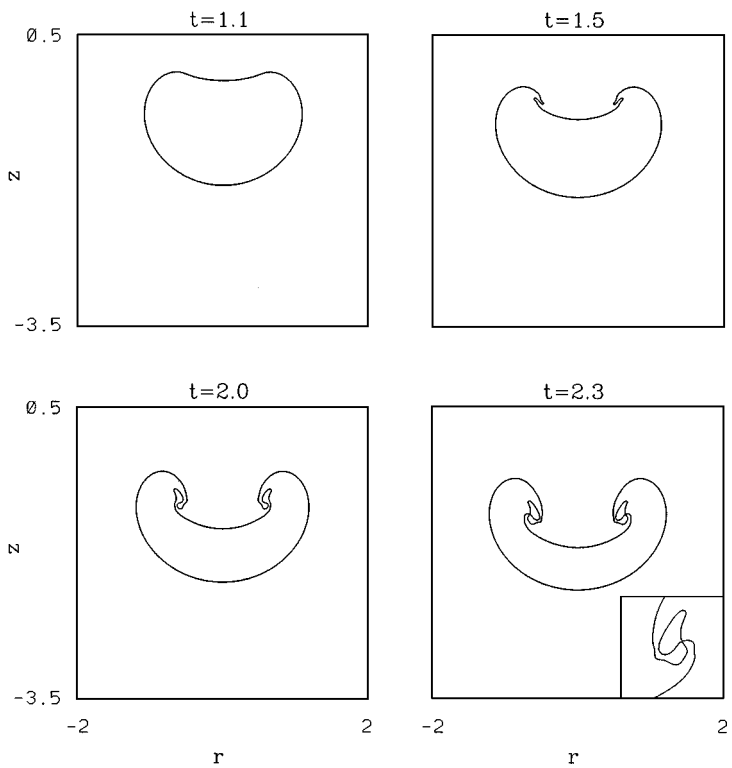

FIG. 6. Evolution of an axisymmetric sheet for $\sigma = 0.01$.

the sheet passes smoothly through the corresponding singularity time for $\sigma = 0$, part of the interface becomes vertical, subsequently rolls up, and produces two fingers as seen at $t = 1.5$. However, these two fingers are much smaller than the previous ones. They grow in length and the tips of fingers broaden and roll with the sheet. By $t = 2.3$, one of the fingers approaches the tail of the other finger and forms a detached blob. The distance between the interfaces is about 3–4 grid sizes at $t = 2.25$ and about only 1–2 grid lengths at $t = 2.3$, which suggests more accuracy may be needed to resolve the solution at these times. Small wiggles (capillary waves) can also be seen.

We next compare the results with the analogous two-dimensional cases. The evolution equations for two-dimensional flows are very similar to Eqs. (1)–(7) except that (r, z) is replaced by (x, y), κ_{mean} by κ, and the normal velocity V_n by its two-dimensional counterpart (HLS94). To avoid confusion between the two-dimensional case and the axisymmetric case, we denote the surface tension coefficient for the two-dimensional case by τ.

Figure 7 shows the evolution of a circle with $\mu(\alpha, 0) = -\cos(\alpha)$ and $\tau = 0.01$ for the two-dimensional case. Even though we do not present the interface at the exact same time for both cases, it is clear that the two evolutions are very similar to each other qualitatively. As seen in the close-ups of Figs. 6 and 7, there are small oscillations near the interaction region which are due to the development of capillary waves (HLS97). However, the oscillations are slightly more pronounced for the axisymmetric case as shown in Fig. 6.

Next we increase σ to 0.1 for the axisymmetric case. For this case as seen in Fig. 8, the sheet oscillates as it translates downward and the evolution of the sheet remains smooth.

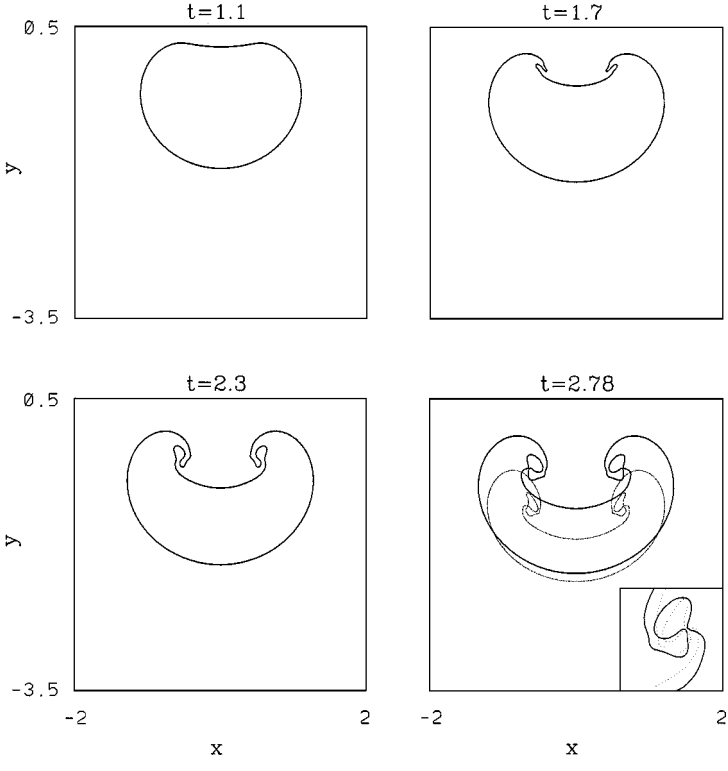

FIG. 7. Evolution of a two-dimensional sheet for $\tau = 0.01$. Dotted line: the corresponding axisymmetric sheet at pinch-off.

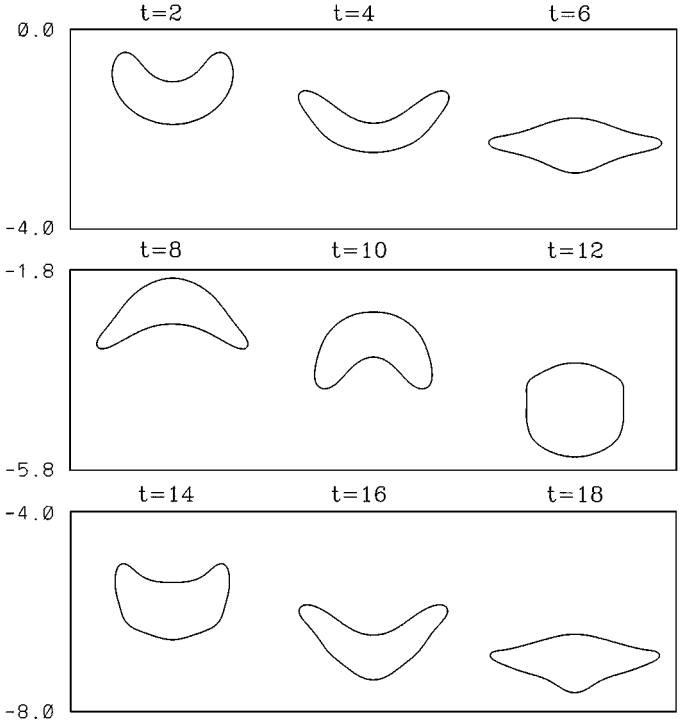

FIG. 8. Evolution of an axisymmetric sheet for $\sigma = 0.1$.

This oscillatory behavior of the sheet with large surface tension is also observed for a periodic open sheet in two-dimensional flows (HLS97).

In Fig. 9, we summarize the results for different values of surface tension. For small surface tensions the sheet self-intersects during roll-up. For medium-sized surface tensions, the sheet pinches on its sides. For large surface tensions there is no pinch-off and the sheet remains smooth. All pinch-offs occur away from the axis of symmetry.

In order to investigate further the effect of surface tension, we next consider a different dipole strength (corresponding to a different vortex sheet strength)

$$\mu(\alpha, 0) = -\cos(2\alpha) \quad \alpha \in [0, \pi] \tag{38}$$

as the initial condition for the axisymmetric flow [23]. In this case, the initial vortex sheet strength is of both positive and negative values for $r > 0$ in contrast to the case (37).

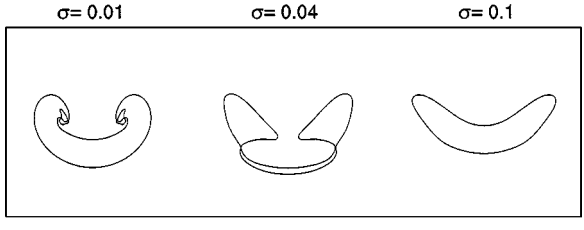

FIG. 9. A summary of the profiles of vortex sheets for different values of surface tension with $\mu(\alpha, 0) = -\cos(\alpha)$.

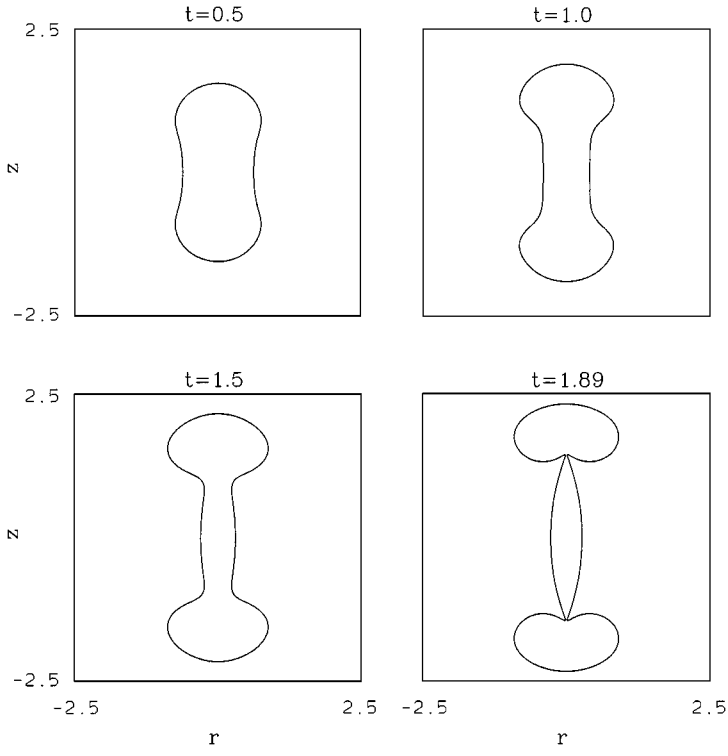

FIG. 10. Evolution of an axisymmetric sheet for $\sigma = 0.2$ and $\mu(\alpha, 0) = -\cos(2\alpha)$.

Figure 10 shows the evolution from a sphere with (38) as the initial condition for the dipole strength for an axisymmetric flow with $\sigma = 0.2$. The calculation starts with $N = 513$ and $\Delta t = 5 \times 10^{-4}$ and is refined up to $N = 2049$ and $\Delta t = 5 \times 10^{-5}$ at $t = 1.89$. Because of the initial vorticity arrangement, the sphere first elongates as the middle part of the sheet (at $z = 0$) moves toward $r = 0$. As the sheet self-approaches, it develops a neck region with the middle point ($z = 0$) moving more slowly than its neighbors. Around $t = 1.89$, the sheet pinches at $r = 0$ and forms satellites.

In Figs. 11 and 12, the mean curvature and vortex sheet strength are plotted as functions of α at different times. At $t = 1.89$, the distance between the sheet around pinching is slightly larger than the corresponding one at $t = 4.85$ in Fig. 1, in which the pinching occurs at $r > 0$. However, the corresponding curvature and vortex sheet strength as seen in Figs. 11 and 12 (notice a different vertical scale at $t = 1.89$) are much larger than those in Figs. 4 and 5. This is consistent with our observation that the case with pinch-off at $r > 0$ can be better resolved numerically than pinch-off at $r = 0$. This additional numerical difficulty is mainly caused by the presence of $1/r$ in the curvature. The large curvature present at pinch-off near $r = 0$ introduces large variation in γ and in the integrands near the axis of symmetry. Consequently, the accurate evaluation of the integrals becomes increasingly difficult.

At $t = 1.89$ (see Fig. 12), the first peak (counting from $\alpha = 0$) of γ corresponds to the location of pinch-off at $z < 0$ for the right part of the sheet. The formation of a concentrated peak of positive circulation around the pinch-off indicates an outward flux of fluid to the satellite drop. This peak also results in an acceleration of the sheet around the pinch-offs. On the other hand, the nearly vanishing vortex sheet strength along the middle part of the sheet

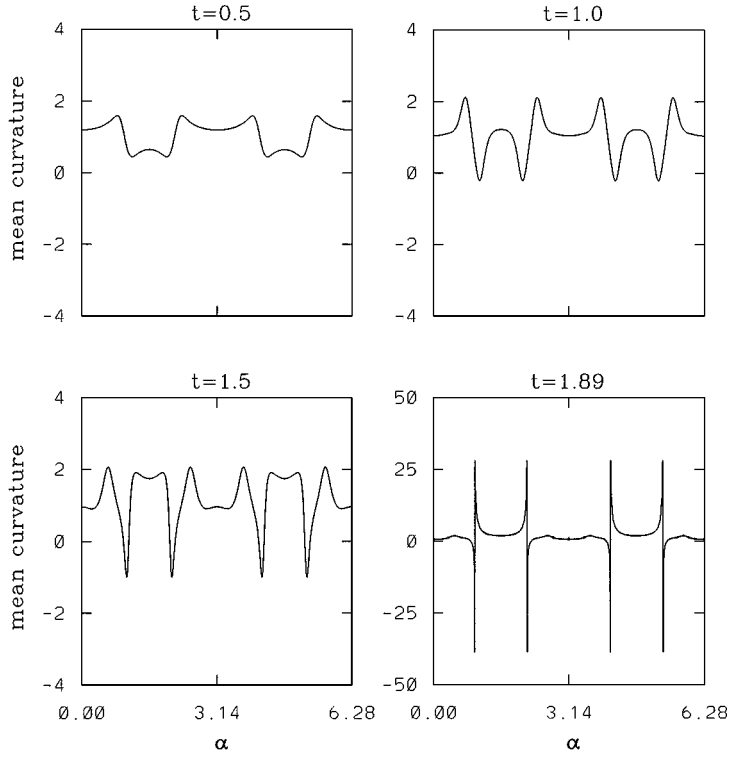

FIG. 11. Mean curvature vs α at different times for $\sigma = 0.2$ and $\mu(\alpha, 0) = -\cos(2\alpha)$.

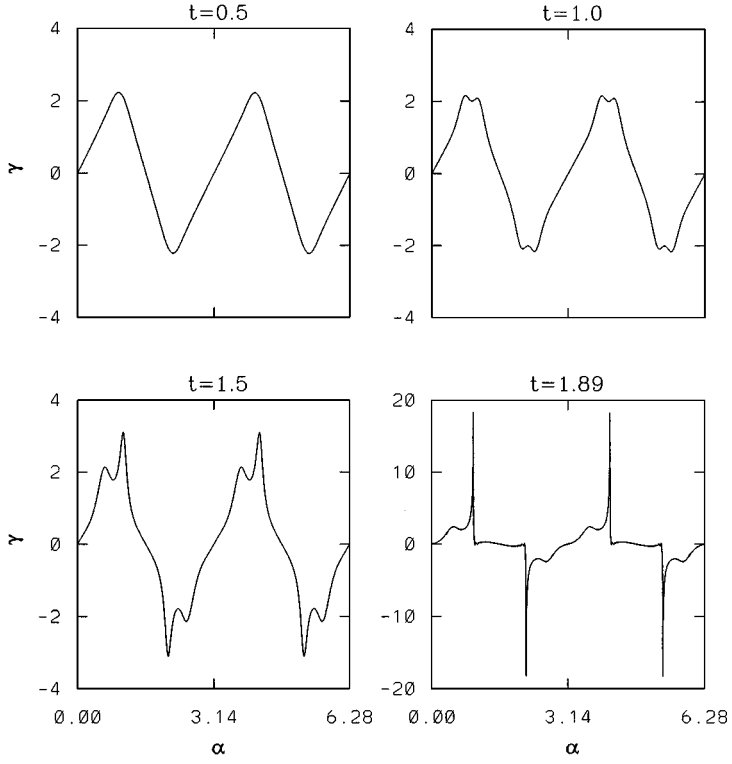

FIG. 12. Vortex sheet strength γ vs α at different times for $\sigma = 0.2$ and $\mu(\alpha, 0) = -\cos(2\alpha)$.

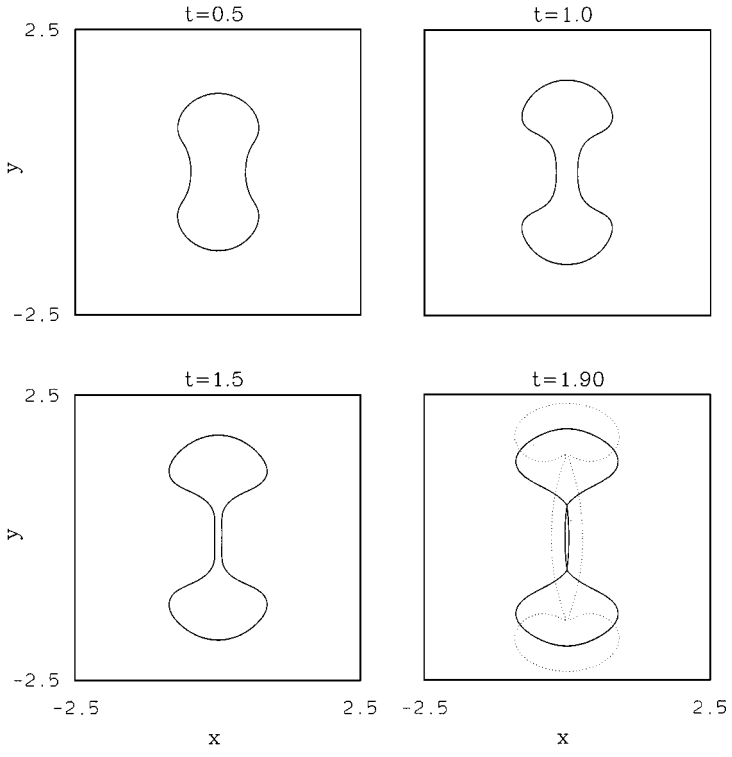

FIG. 13. Evolution of a two-dimensional sheet for $\tau = 0.2$ and $\mu(\alpha, 0) = -\cos(2\alpha)$. Dotted line: the corresponding axisymmetric sheet at pinch-off.

(the part between the two peaks with opposite signs) is responsible for its slower motion. As a result the sheet around the pinching region accelerates to $r = 0$ with the middle part of the sheet left behind, and the formation of a satellite drop becomes inevitable.

The evolution for the analogous two-dimensional flow is shown in Fig. 13 (the same initial condition with $\tau = 0.2$). One of the striking features of the axisymmetric case in Fig. 10 is the overturning of the sheet near the pinching region, i.e., z has multiple values for some fixed $r > 0$, in contrast to the two-dimensional case shown in Fig. 13. In Fig. 14, close-ups of the pinch-offs are plotted for both axisymmetric flows and two-dimensional flows, and the neck distances for both cases are plotted as functions of time as well. Clearly, the axisymmetric vortex sheet accelerates toward pinching more rapidly than its two-dimensional counterpart. As a consequence, the satellite drop that forms in the axisymmetric flow is larger than its two-dimensional counterpart. A detailed study of the pinching requires higher resolution and is currently in progress [41]. Overturning associated with pinch-offs in various fluid flows has been studied in [42–45]. In order to establish simple models for the local behavior of solutions near pinch-off, a priori knowledge of the existence of overturning is necessary [42].

We notice that for the first initial vortex sheet strength (37) the axisymmetric and two-dimensional pinch-offs have similar structures, as demonstrated in Figs. 6 and 7. However, the pinch-offs in Figs. 10 and 13 are less like one another. It should be anticipated that when a pinch-off occurs at $r = 0$ (Fig. 10) or $x = 0$ (Fig. 13) the flow dynamics near the pinch-off region is very different between axisymmetric flows and two-dimensional flows. It is observed that the self-induced velocity near the axis is larger in the axisymmetric case

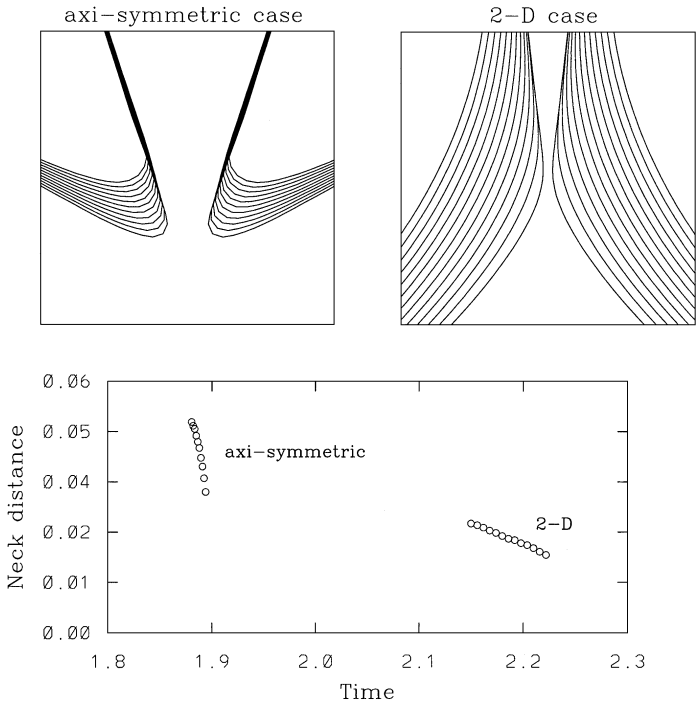

FIG. 14. Close-ups around the pinch-offs for the axisymmetric sheet with $\sigma = 0.2$ and the two-dimensional sheet with $\tau = 0.2$. The axisymmetric sheets are plotted at $t = 1.88 + i \times 0.001$ for $i = 0, \ldots, 10$; the two-dimensional sheets are plotted at $t = 1.66 + i \times 0.02$ for $0 = 0, \ldots, 12$; and the neck distances are plotted as functions of time.

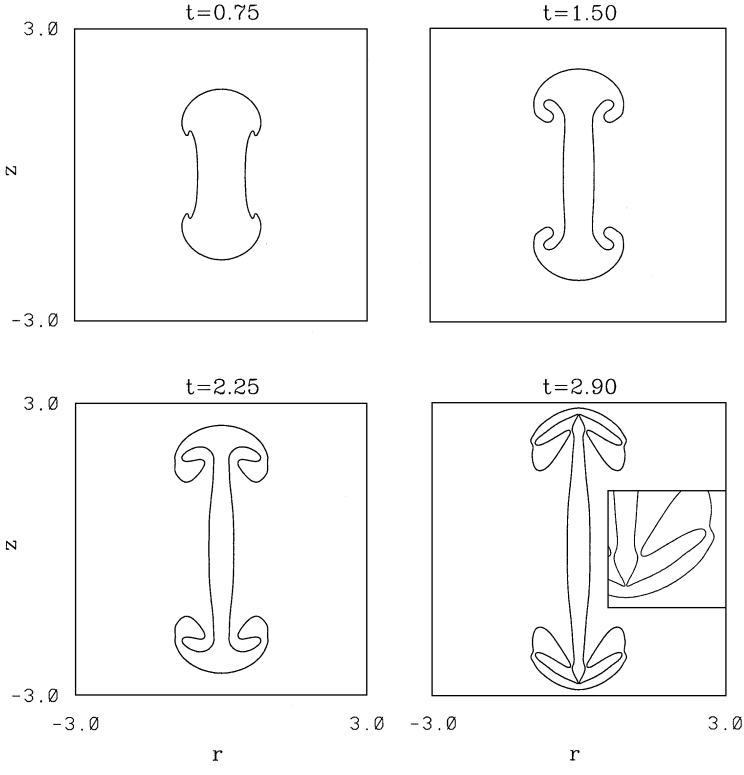

FIG. 15. Evolution of an axisymmetric sheet for $\sigma = 0.04$ and $\mu(\alpha, 0) = -\cos(2\alpha)$.

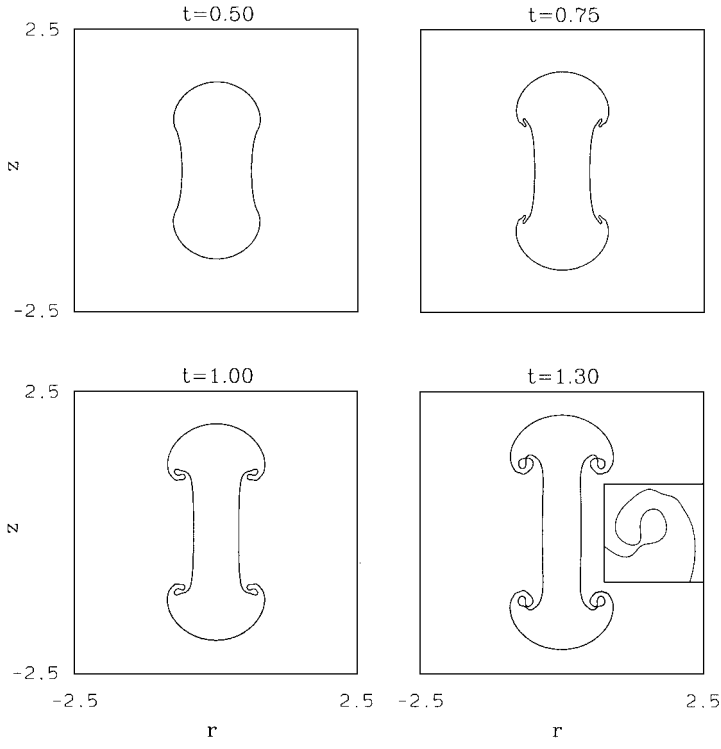

FIG. 16. Evolution of an axisymmetric sheet for $\sigma = 0.02$ and $\mu(\alpha, 0) = -\cos(2\alpha)$.

than in the two-dimensional case, and as a result, stronger local jets develop and accelerate the pinch-off. Consequently there is overturning in the axisymmetric case and not in the two-dimensional case. The reason for the larger self-induced velocity in the axisymmetric case is likely due to the filament curvature, which is large near the axis. Away from the axis, the axisymmetric curvature is closer to the planar one and as a result, the self-induced velocities as well as the shapes of the pinch-offs are more comparable.

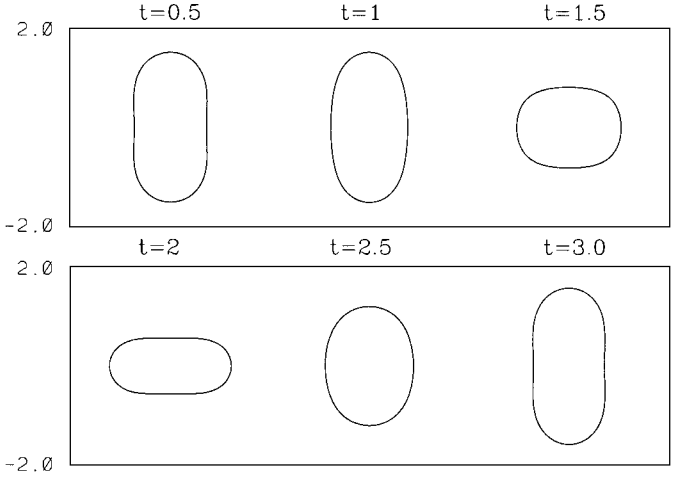

FIG. 17. Evolution of an axisymmetric sheet for $\sigma = 2$ and $\mu(\alpha, 0) = -\cos(2\alpha)$.

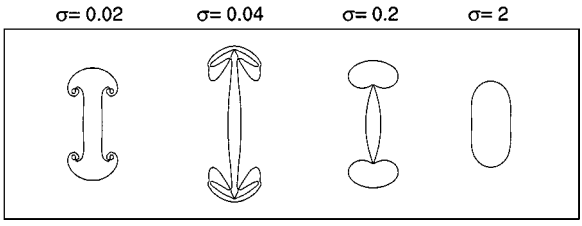

FIG. 18. A summary of the profiles of vortex sheets for different values of of surface tension with $\mu(\alpha, 0) = -\cos(2\alpha)$.

Now we turn our attention back to study the effect of surface tension for axisymmetric flows. We reduce σ by a factor of 5 to $\sigma = 0.04$ with other parameters the same as those in Fig. 10. Figure 15 shows a calculation for $\sigma = 0.04$ with a numerical resolution from $N = 513$ and $\Delta t = 1 \times 10^{-4}$ to $N = 2049$ and $\Delta t = 2 \times 10^{-5}$. At early times (up to around $t = 2.25$), the sheet develops internal roll-up structures that are similar to those observed using (37) with a comparable surface tension. However, unlike Fig. 6 in which the roll-up continues and results in pinching at $r > 0$, the sheet in Fig. 15 forms a thin jet which causes the sheet pinch at $r = 0$ first. During the evolution there is competition between different types of pinch-offs: the two-dimensional pinch-offs (those occurring at $r > 0$) and three-dimensional pinch-offs (at $r = 0$). For this case, the three-dimensional pinch-off wins.

We next reduce the surface tension by a factor of 2 to $\sigma = 0.02$. As shown in Fig. 16, the sheet self-intersects at $r > 0$. The sheet profile at $t = 0.75$ in Fig. 16 is very similar to the profile at $t = 0.5$ in Fig. 15. However, for $\sigma = 0.02$ the sheet develops much smaller fingers afterward. The smaller roll-up structure, which is due to smaller surface tension, leads to continuation of the roll-up and pinch-off at $r > 0$, in contrast to the previous case with the larger surface tension $\sigma = 0.04$.

On the other hand, when the surface tension is sufficiently large, for example, $\sigma = 2$ (see Fig. 17), the sheet remains smooth and oscillates similarly to what is shown in Fig. 8, which uses the first initial vortex sheet strength (37).

In summary, we show the profiles of the sheet in Fig. 18 for different values of surface tension strength when the initial vortex sheet strength (38) is used. For very large surface tensions ($\sigma = 2$), the sheet oscillates. For small surface tensions ($\sigma = 0.02$), the sheet develops a rolled-up structure and self-intersects away from the axis of symmetry. Both cases are similar to the dynamics of analogous two-dimensional flows. On the other hand, for relatively large surface tensions ($\sigma = 0.2$), the sheet necks down and pinch-off occurs at the axis of symmetry, and an overturning of the interface is found. This is not observed for the two-dimensional flows. For moderately sized surface tensions ($\sigma = 0.04$), the sheet evolves via a combination of spirals, necks, and pinch-offs.

5. CONCLUSIONS AND DISCUSSIONS

In order to simulate the evolution of free surfaces in axisymmetric flows, there are two major computational challenges: (1) the accurate evaluation of the boundary integrals and (2) the strong stability constraints associated with the presence of surface tension. By combining adaptive quadratures with the *small-scale decomposition* technique, we have developed an accurate and efficient computational method of computing the motion of vortex sheet with surface tension in axisymmetric flows. In particular, using this method we have investigated

the effect of surface tension on the evolution of vortex sheets in axisymmetric flows. As shown in Figs. 9 and 18, which illustrate the solutions at pinch-off for different values of surface tension, we observe that the interface may form either spirals or necks or may form a combination of these structures at pinch-off.

We anticipate that similar computational methods can be developed for other free-surface motions in axisymmetric flows, such as the motion of drops [28] or porous media flows [30]. Also it would be interesting to compare different strategies for evaluating the boundary integrals, such as [19, 30], for free-surface flows with or without surface tension.

ACKNOWLEDGMENTS

It is a pleasure to thank G. Baker, T. Hou, J. Lowengrub, and M. Shelley for helpful and interesting discussions concerning this work. I am grateful to J. Lowengrub for his help and suggestions during the preparation of the manuscript. Also, I thank the referee for suggestions for improving the article. This work was partially supported by National Science Foundation Grant DMS 0074414.

REFERENCES

1. P. Saffman and G. Baker, Vortex interactions, *Annu. Rev. Fluid Mech.* **11**, 95 (1979).
2. G. R. Baker, D. I. Meiron, and S. A. Orszag, Generalized vortex methods for free-surface flow problems, *J. Fluid Mech.* **123**, 477 (1982).
3. C. Pozrikidis, *Boundary Integral and Singularity Methods for Linearized Viscous Flow* (Cambridge Univ. Press, Cambridge, UK, 1992).
4. T. Hou, J. Lowengrub, and M. Shelley, Boundary integral methods for multicomponent fluids and multiphase materials, *J. Comput. Phys.* **169**, 302 (2001).
5. G. R. Baker and D. W. Moore, The rise and distortion of a two-dimensional gas bubble in an inviscid liquid, *Phys. Fluids* **A1**, 1451 (1989).
6. R. Zalosh, Discretized simulation of vortex sheet evolution with buoyancy and surface tension effects, *AIAA J.* **14**, 1575 (1976).
7. D. I. Pullin, Numerical studies of surface tension effects in nonlinear Kelvin–Helmholtz and Rayleigh–Taylor singularities, *J. Fluid Mech.* **244**, 507 (1992).
8. R. Rangel and W. Sirignano, Nonlinear growth of Kelvin–Helmholtz instability: Effect of surface tension and density ratio, *Phys. Fluids* **31**, 1845 (1988).
9. G. R. Baker and A. Nachbin, Stable methods for vortex sheet motion in the presence of surface tension, *SIAM J. Sci. Comput.* **19**, No. 5, 1737 (1998).
10. T. Hou, J. Lowengrub, and M. Shelley, Removing the stiffness from interfacial flows with surface tension, *J. Comput. Phys.* **114**, 312 (1994).
11. T. Hou, J. Lowengrub, and M. Shelley, The long-time motion of vortex sheets with surface tension, *Phys. Fluids* **9**, No. 7, 1933 (1997).
12. H. Kudela, The influence of surface tension effects using vortex method in the study of Rayleigh–Taylor instability, in *Notes on Numerical Fluids Mechanics* (1990).
13. H. Ceniceros and T. Hou, Convergence of a nonstiff boundary integral method for interfacial flows with surface tension, *Math Comput.* **67**, 137 (1998).
14. H. Ceniceros and T. Hou, Dynamic generation of capillary waves, *Phys. Fluids* **11**, 1042 (1999).
15. J. Beale, T. Hou, and J. Lowengrub, Growth rates for the linear motion of fluids interfaces far from equilibrium, *Comm. Pure Appl. Math.* **46**, 1269 (1993).
16. J. Beale, T. Hou, and J. Lowengrub, Convergence of boundary integral methods for water waves with and without surface tension, *SIMA J. Numer. Anal.* **33**, 1797 (1996).
17. D. A. Pugh, *Development of Vortex Sheets in Boussinesq Flows-Formation of Singularities*, Ph.D. thesis (Imperial College of Science and Technology, 1989).

18. Q. Nie and G. R. Baker, Application of adaptive quadrature to axi-symmetric vortex sheet motion, *J. Comput. Phys.* **143**, 49 (1998).
19. M. Nitsche, Axi-symmetric vortex sheet motion: Accurate evaluation of the principal value integral, *SIAM J. Sci. Comput.* **21**, No. 3, 1066 (1999).
20. T. Ishihara and Y. Kaneda, Singularity formation in three-dimensional motion of a vortex sheet, *J. Fluids Mech.* **300**, 339 (1995).
21. M. Brady and D. I. Pullin, On singularity formation in three-dimensional vortex sheet evolution, *Phys. Fluids* **11**, No. 11, 3198 (1999).
22. M. Nitsche, *Singularity Formation in a Cylindrical and a Spherical Vortex Sheet*, Preprint (2001).
23. G. R. Baker and Q. Nie, *Singularity Formation in Axi-Symmetric Vortex Sheets*, In preparation.
24. G. R. Baker, D. I. Meiron, and S. A. Orszag, Boundary integral methods for axisymmetric and three-dimensional Rayleigh–Taylor instability problems, *Physical D* **12**, 19 (1984).
25. B. Bernadinis and D. W. Moore, A ring-vortex representation of an axi-symmetric vortex sheet, in *Studies of Vortex Dominated Flows* (Springer-Verlag, Berlin/New York, 1987), p. 33.
26. A. Sidi and M. Israeli, Quadrature methods for singular and weakly fredholm integral equations, *J. Sci. Comput.* **3**, 201 (1988).
27. D. Dommermuth and D. Yue, Numerical simulations of nonlinear axi-symmetric flows with a free-surface, *J. Fluid Mech.* **178**, 195 (1987).
28. T. S. Lundgren and N. N. Mansour, Oscillations of drops in zero gravity with weak viscous effects, *J. Fluid Mech.* **194**, 479 (1988).
29. O. Hasan and A. Prosperetti, Bubble entrainment by the impact of drops on liquid surfaces, *J. Fluid Mech.* **1219**, 143 (1990).
30. H. Ceniceros and H. Si, Computation of axi-symmetric suction flow through poros media in the presence of surface tension, *J. Comput. Phys.* **165**, 237 (2000).
31. R. E. Caflisch and Xiao-Fan Li, Lagrangian theory for 3D vortex sheets with axial or helical symmetry, *Transport Theory Stat. Phys.* **21**, 559 (1992).
32. A. S. Kronrod, *Nodes and Weights of Quadrature Formulas* (Consultants Bureau, New York, 1965).
33. T. N. Patterson, The optimum addition of points to quadrature formulae, *Math. Comput.* **22**, 847 (1968).
34. R. Piessens, E. de Doncker-Kapenga, C. W. Uberhuber, and D. K. Kahaner. *Quadpack* (Springer-Verlag, Berlin/New York, 1983).
35. Paul F. Byrd and Morris D. Friedman, *Handbook of Elliptic Integrals for Engineers and Physicists* (Springer-Verlag, Berlin/New York, 1953).
36. C. Clenshaw and A. R. Curtis, A method for numerical integration on an automatic computer, *Numer. Math.* **12**, 197 (1960).
37. R. Piessens and M. Branders, The evaluation and application of some modified moments, *BIT* **13**, 443 (1973).
38. M. J. Shelley and G. R. Baker, Order conserving approximation to derivatives of periodic function using iterated splines, *SIAM J. Numer. Anal.* **25**, 1442 (1988).
39. R. Krasny, A study of singularity formation in a vortex sheet by the point vortex approximation, *J. Fluid Mech.* **167**, 65 (1986).
40. M. Nitsche, Evolution of a cylindrical and spherical vortex sheet, in *Proceedings of Second International Workshop on Vortex Flows and Related Numerical Methods, 1995*.
41. J. Lowengrub and Q. Nie, The long-time motion of vortex sheets with surface tension in axi-symmetric flows, In preparation.
42. J. Eggers, Nonlinear dynamics and breakup of free-surface flows, *Rev. Modern Phys.* **69**, No. 3, 865 (1997).
43. R. Day, J. Hinch, and J. Lister, Self-similar capillary pinchoff of an inviscid fluid, *Phys. Rev. Lett.* **80**, 704 (1998).
44. E. Wilkes, S. Phillips, and O. Basaran, Computational and experimental analysis of dynamics of drop formation, *Phys. Fluids* **11**, No. 12, 3577 (1999).
45. P. Notz, A. Chen, and O. Basaran, Satellite drops: Unexpected dynamics and change of scaling during pinch-off, *Phys. Fluids* **13**, No. 3, 549 (2001).